Blocking polysulfide by physical confinement and catalytic conversion of SiO$_2$@MXene for Li–S battery

Chaoyue Zhang; Junan Feng; Xin Guo ⓘ ; Jinqiang Zhang; Wenxue Zhang ⓘ ; Lixue Zhang; Jianjun Song ✉ ⓘ ; Guangjie Shao ✉ ; Guoxiu Wang ✉ ⓘ

Check for updates

View Online   Export Citation   CrossMark

Blocking polysulfide by physical confinement and catalytic conversion of SiO$_2$@MXene for Li–S battery Ⓕ

View Online   Export Citation   CrossMark

Chaoyue Zhang,[1,2] Junan Feng,[1] Xin Guo,[3] (iD) Jinqiang Zhang,[3] Wenxue Zhang,[4] (iD) Lixue Zhang,[2] Jianjun Song,[1,a)] (iD) Guangjie Shao,[5,a)] and Guoxiu Wang[3,a)] (iD)

AFFILIATIONS

[1]College of Physics, Qingdao University, Qingdao 266071, China
[2]College of Chemistry and Chemical Engineering, Qingdao University, Qingdao 266071, China
[3]Centre for Clean Energy Technology, Faculty of Science, University of Technology Sydney, Sydney, New South Wales 2007, Australia
[4]State Key Laboratory of Metastable Materials Science and Technology, Yanshan University, Qinhuangdao 066004, China
[5]School of Materials Science and Engineering, Chang'an University, Xi'an 710064, China

[a)]Author to whom correspondence should be addressed: jianjun.song@qdu.edu.cn; shaoguangjie@ysu.edu.cn; and Guoxiu.Wang@uts.edu.au

ABSTRACT

Lithium–sulfur (Li–S) batteries have attracted increasing attention for next-generation energy storage systems with a high energy density and low cost. However, the practical applications have been plagued by the sluggish reaction kinetics and the shuttle effect of lithium polysulfides (LiPSs). Herein, core–shell SiO$_2$@Ti$_3$C$_2$T$_x$ MXene (SiO$_2$@MX) hollow spheres are constructed as multifunctional catalysts to boost the performance of Li–S batteries. The dual-polar and dual-physical properties of SiO$_2$ core and MXene shell provide multiple defense lines to the shuttle effect by chemical and physical confinement to LiPSs. Density functional theory calculations prove that Ti$_3$C$_2$T$_x$ MXene and SiO$_2$ enable the stronger trapping ability of LiPSs and the fast Li$_2$S decomposition process. With this strategy, the robust SiO$_2$@MX/S electrodes deliver superior electrochemical performances, including a high capacity of 1263 mAh g^{-1}, and remarkable cycling stability with an ultralow capacity decay of 0.04% per cycle over 1000 cycles at 1 C. This work highlights the significance of core-shell dual-polar structural sulfur catalysts for practical application in advanced Li–S batteries.

Published under an exclusive license by AIP Publishing. https://doi.org/10.1063/5.0147522

Rechargeable lithium–sulfur (Li–S) batteries have been considered one of the most promising battery systems because of the natural abundance of sulfur, high specific energy density (2600 Wh kg^{-1}), and high theoretical capacity (1675 mAh g^{-1}).[1] Despite attractive promises, there are still several serious issues impeding the practical application: (1) the extra-low electronic conductivity of sulfur and its discharge products (Li$_2$S$_2$/Li$_2$S); (2) the shuttle effect of lithium polysulfides (Li$_2$S$_x$, $4 \leq x \leq 8$); (3) the low redox reaction kinetics of LiPSs; and (4) rigorous volumetric expansion of sulfur. These issues undesirably result in low sulfur utilization, poor rate performance, and severe capacity decay.[2,3]

To address these problems, designing trapping and catalyzing typed polar compounds as sulfur hosts have been a popular strategy to ensure efficient chemical interactions and electrochemical catalytic abilities for the conversion of LiPSs to Li$_2$S, which plays a crucial role

to inhibit the shuttle effect in Li–S batteries.[4–8] Among these functional hosts, the porous hollow structural oxides have been widely employed owing to the advantages of facile preparation, controllable 3D nano-architecture, and low cost.[9,10] Nevertheless, most of them usually possess poor conductivity, leading to low sulfur utilization, and the hollow structure inevitably provides channels for the shuttle of lithium polysulfide. Therefore, further modification of polar hollow oxides to enhance the electricity and block the diffusion channel of LiPSs becomes essential for advanced Li–S batteries.[11]

Recently, Ti-based MXene has been extensively studied in Li–S batteries, demonstrating its promising advantages, such as outstanding conductivity, 2D polar surface, physical barrier, and catalytic conversion ability.[12–16] Herein, we report an architecture of dual-polar core–shell SiO$_2$@Ti$_3$C$_2$T$_x$ MXene (SiO$_2$@MX) hollow spheres prepared by an electrostatic self-assembly strategy as multifunctional sulfur host to

boost the performance of Li–S batteries. The unique core-shelled structure provides dual-chemical and dual-physical barriers to maximize the capture of LPSs within the cathode. MXene enhances electron transfer and accelerates redox kinetics by bi-directional selective catalysis for the oxidation and reduction processes of LiPSs. When used as cathodes for Li–S batteries, the SiO_2@MX/S hybrid electrodes exhibit a high capacity, remarkable long-term cycling stability, and excellent cycling performance at high sulfur loading.

Figure 1(a) illustrates the synthesis strategy of the core–shell structural SiO_2@MX hollow sphere. The SEM and TEM images [Figs. S1(a)–S1(d)] show that polystyrene (PS) spheres are highly uniform with smooth surfaces. After coating the SiO_2 layer, the surface becomes rough due to the coverage of SiO_2 nanoparticles [Figs. S1(e)–S1(h)]. Subsequently, aminopropyl-trimethoxysilane was employed to regulate the surface charge of PS@SiO_2, and then the PS@SiO_2@MX

FIG. 1. (a) Schematic of the preparation process of SiO_2@MX hollow sphere. SEM images of PS@SiO_2@MX spheres (b) and SiO_2@MX hollow spheres (c). (d) and (e) TEM images of SiO_2@MX hollow spheres. (f) SEM image and EDS mapping: Si, O, and Ti elemental distribution of SiO_2@MX hollow spheres. (g)–(j) High-resolution XPS spectra of Si 2p, O 2p, C 1s, and Ti 2p of SiO_2@MX host.

microspheres (Figs. S2 and S3) were obtained by the electrostatic self-assembly interaction between amine-functionalized PS@SiO_2 and $Ti_3C_2T_x$ MXene dispersion. Figure 1(b) clearly shows that PS@SiO_2@MX well maintains the spherical morphology, and ultrathin $Ti_3C_2T_x$ sheets encapsulate on the surface of PS@SiO_2, proving the coupling between PS@SiO_2 and MXene. Then, the PS@SiO_2 and PS@SiO_2@MX are annealed at 450 °C for 4 h under Ar atmosphere, and PS will be decomposed to form the hollow sphere structure. The SEM [Figs. 1(c) and S4] confirms the hollow structure of SiO_2@MX and SiO_2 spheres. TEM images [Figs. 1(d) and 1(e)] show that the SiO_2 hollow spheres are composed of small nanoparticles and then are enclosed by MXene sheets, which are almost transparent under the electron beam, and the thickness of SiO_2 can be found to be about 45–50 nm. EDS mapping spectrum [Fig. 1(f)] of SiO_2@MX shows the uniform distribution of Si, O, and Ti elements on a large scale. The results fully suggest the synthesis of dual-polar core-shelled SiO_2@MX architecture.

High-resolution XPS spectra of Si 2p [Fig. 2(g)] of the SiO_2@MX show a peak at a binding energy of 104.0 eV, corresponding to Si^{4+} species in SiO_2. The O 2p spectra [Fig. 2(h)] can be fitted to three peaks at 529.8, 531.0, and 533.3 eV, which can be assigned to Ti–O_x, C–O/OH, and Si–O, respectively. In Fig. 2(i), the C 1s signal of SiO_2@MX has deconvoluted into several signals that appeared at 288.5, 286.0, 284.3, and 287.1 eV corresponding to C=C, C−O, C−C, and Ti–C bonds, respectively. In Ti 2p spectrum [Fig. 2(j)], the Ti 2p spectrum mainly consists of Ti $2p_{3/2}$ and Ti $2p_{1/2}$ peaks, the fitted peaks at 454.8 and 461.2 correspond to the Ti−C and Ti−F bonds of MXene, respectively, and the signals at 455.6 and 456.5 correspond to Ti^{2+} and Ti^{3+}, respectively, which are the coordinately unsaturated Ti atoms.[17] The signals located at 458.6 and 463.9 eV correspond to Ti^{4+}(Ti−O). The absence of Ti−O bonds and unsaturated Ti atoms originate from the few oxides (TiO_2) and oxygen-based groups that exist in $Ti_3C_2T_x$ MXene.[18]

SiO_2@MX/S and SiO_2/S were prepared by a modified vapor phase infusion method [Figs. 2(a) and Fig. S5]. EDS mapping images [Fig. 2(b)], linear scan analysis [Fig. 2(c)], and XRD pattern (Fig. S6) of the SiO_2@MX/S composite confirm the loading of sulfur. The contents of sulfur in the SiO_2@MX/S and SiO_2/S cathodes are estimated to be 78% and 75% according to thermogravimetry (TG) analysis, respectively [Fig. 2(d)]. The high-resolution S 2p spectrum [Fig. 2(e)] of SiO_2@MX/S shows two peaks at 164.6 and 163.4 eV, demonstrating the existence of elemental sulfur (S_8) in the composites. The Ti 2p spectrum [Fig. 2(f)] of SiO_2@MX/S shows similar peaks to the Ti 2p of SiO_2@MX, proving the good preservation of $Ti_3C_2T_x$ MXene after the sulfur loading process.

The electrochemical impedance spectroscopy (EIS) in Fig. 3(a) shows the SiO_2@MX/S cathode possesses smaller charge transfer resistance (R_{ct}) compared to the SiO_2/S electrode owing to the highly conductive MXene coordinating with the affinity of the polar SiO_2. Figure 3(b) shows the CV curves of the initial three cycles for SiO_2@MX/S electrode at a scan rate of 0.1 mV s^{-1}. The well-overlapping CV curves indicate the excellent reversibility in the redox process of SiO_2@MX/S electrode, and the higher peak current intensity than that of SiO_2/S cathode (Fig. S7) proves the better redox reaction kinetics of LPSs. The rate capability [Fig. 3(c)] of SiO_2@MX/S and SiO_2/S electrodes shows that the Li–S batteries with SiO_2@MX/S cathode delivered higher discharge-specific capacities (1263.0 mAh g^{-1} at 0.2 C, 1035.1 mAh g^{-1} at 0.5 C, 918.8 mAh g^{-1} at 1 C, and 829.3 mAh g^{-1} at 2 C)

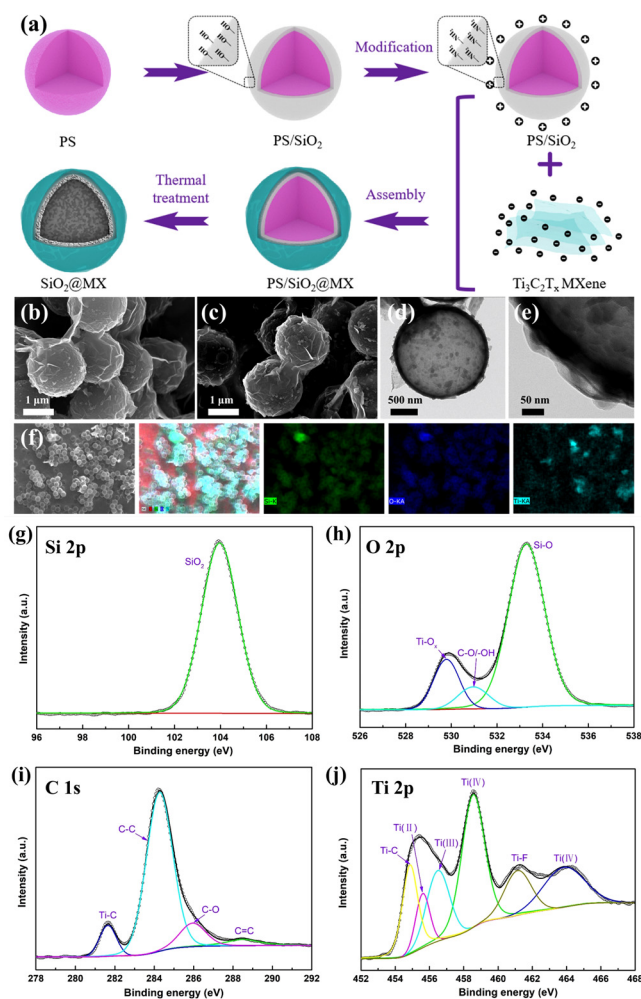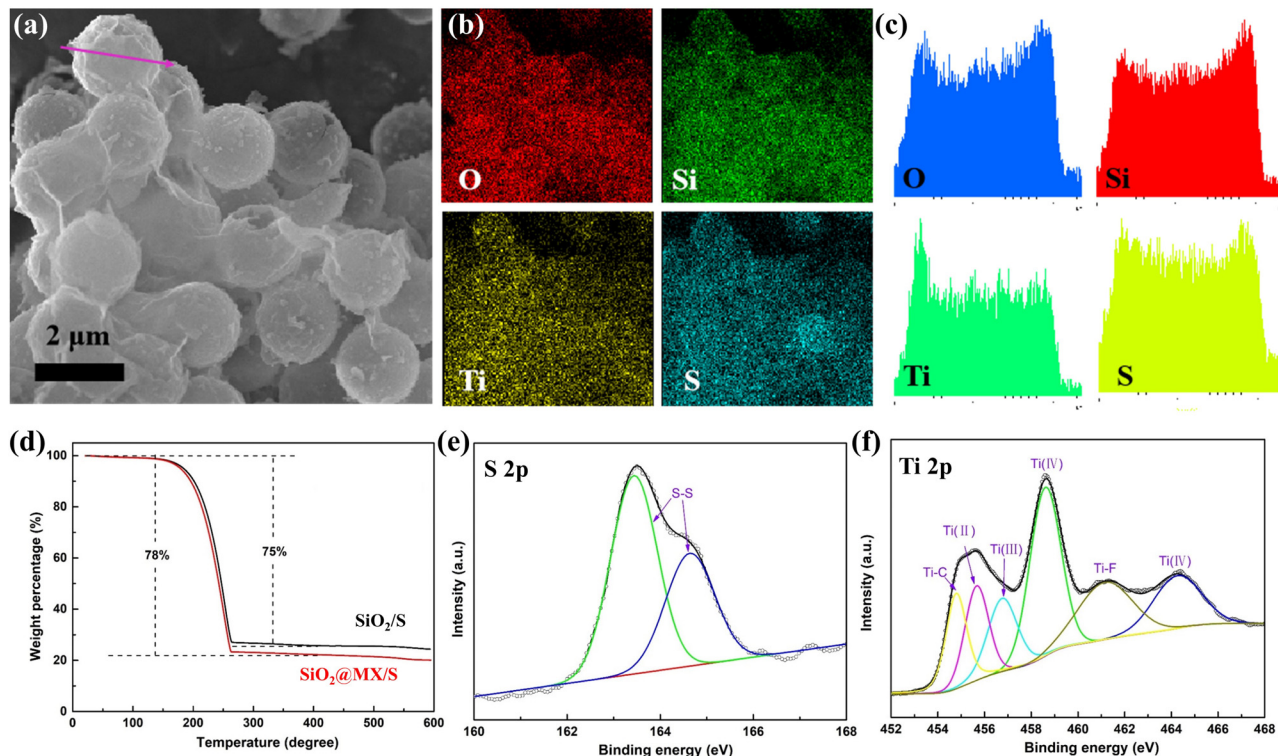**FIG. 2.** SEM image (a), EDS mapping (b), and linear distributions (c) of Si, O, Ti, and S of SiO₂@MX/S composites. (d) TGA analysis of the SiO₂@MX/S and SiO₂/S composites. (e) and (f) High-resolution XPS spectra of S 2p and Ti 2p of SiO₂@MX/S composites.

compared with SiO$_2$/S at each current density. The galvanostatic charge/discharge profiles of SiO$_2$@MX/S cathode in Fig. 3(d) show a much flatter plateau and lower polarization compared to those of SiO$_2$/S cathode (Fig. S8) from 0.2 to 2 C, reflecting its faster redox kinetics. Figure 3(e) shows that the SiO$_2$@MX/S cathode exhibits more stable cycling stability than SiO$_2$/S at 0.2 C, demonstrating that the encapsulation of MXene can effectively restrict the shuttle effect. SiO$_2$@MX/S electrode also shows more stable long-term cycling performance than that of SiO$_2$/S (Fig. S9), which exhibits a high initial capacity of 891.2 mAh g^{-1} with an ultralow capacity decay of 0.04% per cycle over 1000 cycles at 1 C. The cycling stability of SiO$_2$@MX/S at a high rate of 2 C was also tested and shown in Fig. 3(f). After activating at 0.2 C, the SiO$_2$@MX/S cathode presents an initial discharge capacity of 709.3 mAh g^{-1} and a capacity of 488.8 mAh g^{-1} after 500 cycles with a low-capacity decay of 0.057% per cycle and a high average coulombic efficiency of 98.8%. The SiO$_2$@MX/S cathode under high S loading (3.6 mg cm^{-2}) obtains a high initial capacity of 1083.4 mAh g^{-1} and a final discharge capacity of 791.6 mAh g^{-1} along with remarkable cycling stability at a current density of 0.2 C for 100 cycles [Figs. 3(g) and S10]. All these results demonstrate the great promise of multifunctional SiO$_2$@MX host in developing high energy density Li–S batteries for future practical applications.

The Li$_2$S$_6$-symmetrical cells that were assembled with SiO$_2$@MX and SiO$_2$ electrodes were used to verify the improvement of sulfur redox reaction. As shown in Fig. 4(a), the larger current response on CV curves of SiO$_2$@MX indicates that the redox kinetics of the

liquid–liquid phase is significantly enhanced. The reduction process of polysulfides to Li$_2$S was studied by the electrostatic potential discharging method [Figs. 4(b) and 4(c)].[19] Impressively, the SiO$_2$@MX electrode exhibits sharper current peaks, an earlier time of current peak emerged (4425 s), and a larger precipitation capacity of 158.5 mAh g^{-1} compared with the SiO$_2$ cathode (5284 s and 94.5 mAh g^{-1}). Furthermore, the curves of the inverse oxidation decomposition process for Li$_2$S shown in Figs. S11(a) and S11(b) also show that the SiO$_2$@MX delivered higher current peaks, shorter beginning decomposition time (3093 s), and larger decomposition capacity (473.1 mAh g^{-1}) compared with SiO$_2$ cathode, demonstrating the effective bi-directional selective catalysis of SiO$_2$@MX for oxidation and reduction processes.

The Li$_2$S$_6$ adsorption test was performed by soaking 25 mg of SiO$_2$ or SiO$_2$@MX in 2 mM Li$_2$S$_6$ solution. After adsorption, the color of the supernatant with the SiO$_2$@MX composites appears almost transparent after 6 h of uniform mixing [the inset in Fig. 3(d)], highlighting the excellent anchoring ability after coupling MXene. UV/vis absorption measurements further confirm a lower Li$_2$S$_6$ concentration of SiO$_2$@MX composites than SiO$_2$ after soaking Li$_2$S$_6$ solution [Fig. 4(d)]. Density functional theory (DFT) calculation was implemented to show the adsorption energy to further confirm the capture ability of SiO$_2$ and Ti$_3$C$_2$T$_x$ MXene to Li$_2$S$_4$ [Figs. 4(e)–4(i) and Table S1]. The SiO$_2$ possesses an adsorption energy of −6.616 eV with Li$_2$S$_4$, and Ti$_3$C$_2$ exhibits higher adsorption energy of −10.459 eV, indicating their stronger capture ability to LiPSs via the
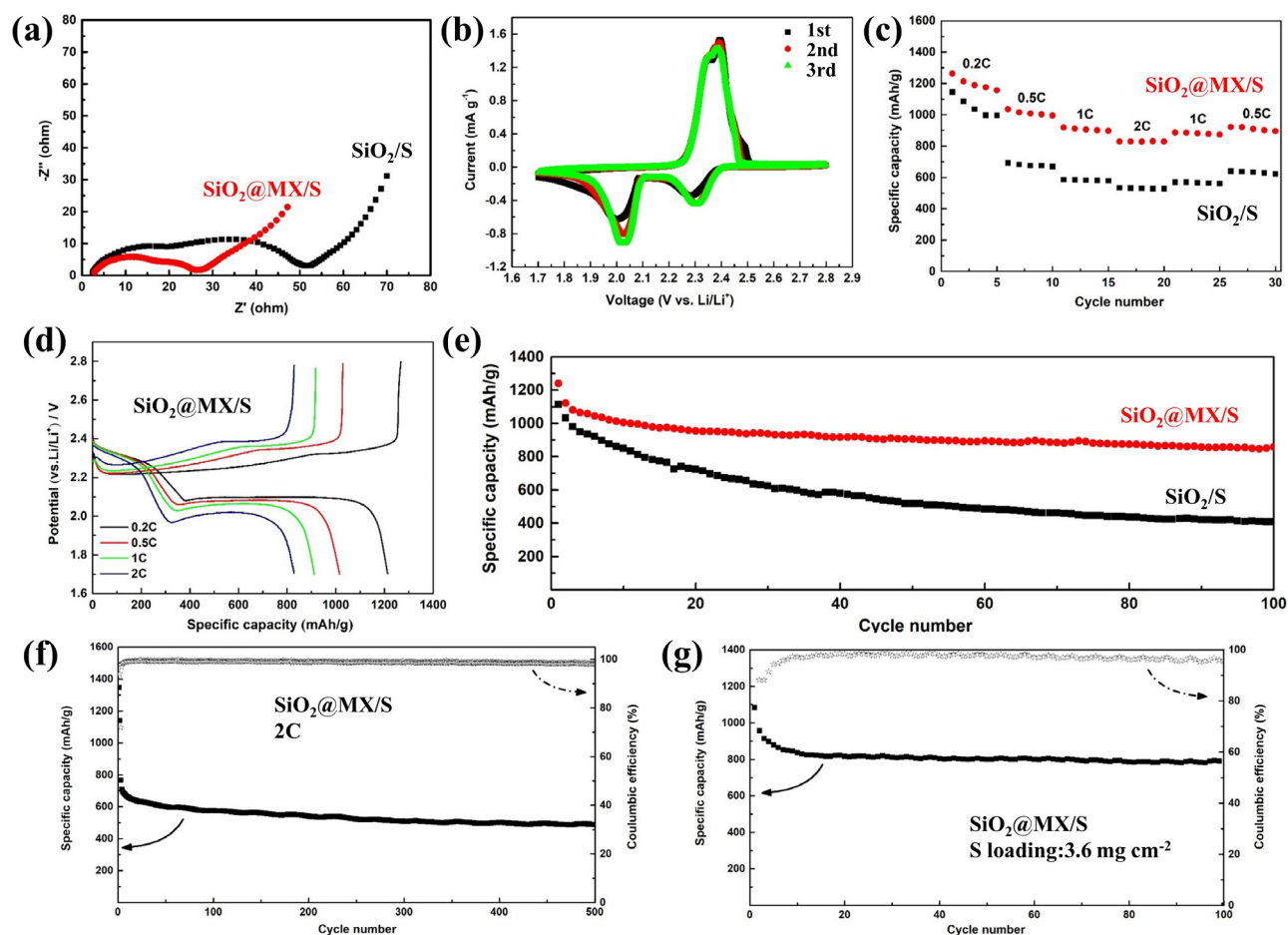
FIG. 3. (a) EIS curves of fresh Li–S batteries with $SiO_2@MX/S$ and SiO_2/S cathodes, (b) CV profiles of Li–S batteries with $SiO_2@MX/S$ cathode with a scan rate of 0.1 mV s^{-1} for three cycles. (c) Rate performance, (d) discharging/charging profiles, (e) cycling performance at 0.2 C, (f) long-term cycling performance at 2 C, and (g) cycling performance under high S loading of 3.6 mg cm^{-2} at 0.2 C.

chemical interaction. When the Ti atoms on the surface are replaced by $-OH$, $-F$, or $-O$ functional groups, the interaction with Li_2S_4 is weakened with the adsorption energy of -2.591, -1.238, and -2.793 eV, respectively, which still shows stronger adsorption energy than that of DME and DOL solvent molecule in the electrolyte (E_{ads} for DME is -0.851 eV and E_{ads} for DOL is -0.693 eV, Table S2) in Fig. S12. Therefore, theoretical results indicate that the LiPSs tend to remain in the dual-polar $SiO_2@MX$ host instead of dissolving into the electrolyte, thus restricting the shuttle effect and enhancing the cycling stability. The Gibbs reaction energy of Li_2S decomposition was also calculated to evaluate the catalytic role of $SiO_2@MX$ electrocatalyst on the conversion of Li_2S. The Ti_3C_2 MXene shows a lower energy barrier (0.464 eV) of Li_2S decomposition than that of SiO_2 (0.607 eV), indicating the accelerated reaction kinetics by the introduction of MXene [Figs. 4(j) and 4(k)]. The experimental and theoretical results consistently prove the strong anchor ability and bi-directional catalyzing property of $SiO_2@MX$ to the conversion of polysulfides.

The performance of simply mixed SiO_2 and MXene composites (M-SiO_2-MX/S) as sulfur hosts was also evaluated (Fig. S13), and the results highly prove the unique superiority of the designed dual-polar core–shell structure [Figs. S14–S17]. Therefore, the superior electrochemical performance of $SiO_2@MX/S$ electrodes is attributed to the following factors (Fig. 5): (1) the SiO_2 core and MXene shell in this structure provide dual-physical and dual-chemical barriers to maximize the capture of LPSs within the cathode, (2) MXene not only promotes the electron transfer but also accelerates the redox kinetics by catalyzing the conversion of LiPSs, and (3) the hollow structure facilitates fast ion diffusion, ensures the sulfur loading, and alleviates the volume expansion.

In summary, we present core-shelled dual-polar $SiO_2@MX$ hollow spheres as multifunctional catalysts to enhance the performance of Li–S batteries. Experimentally and theoretically, we proved that the core-shelled hollow structure is promising to restrict the shuttle effect, and that the $Ti_3C_2T_x$ MXene can boost the redox kinetics by catalyzing the conversion of LiPSs. Benefiting from the synergistic polysulfides capture and efficient catalytic conversion between SiO_2 and MXene in
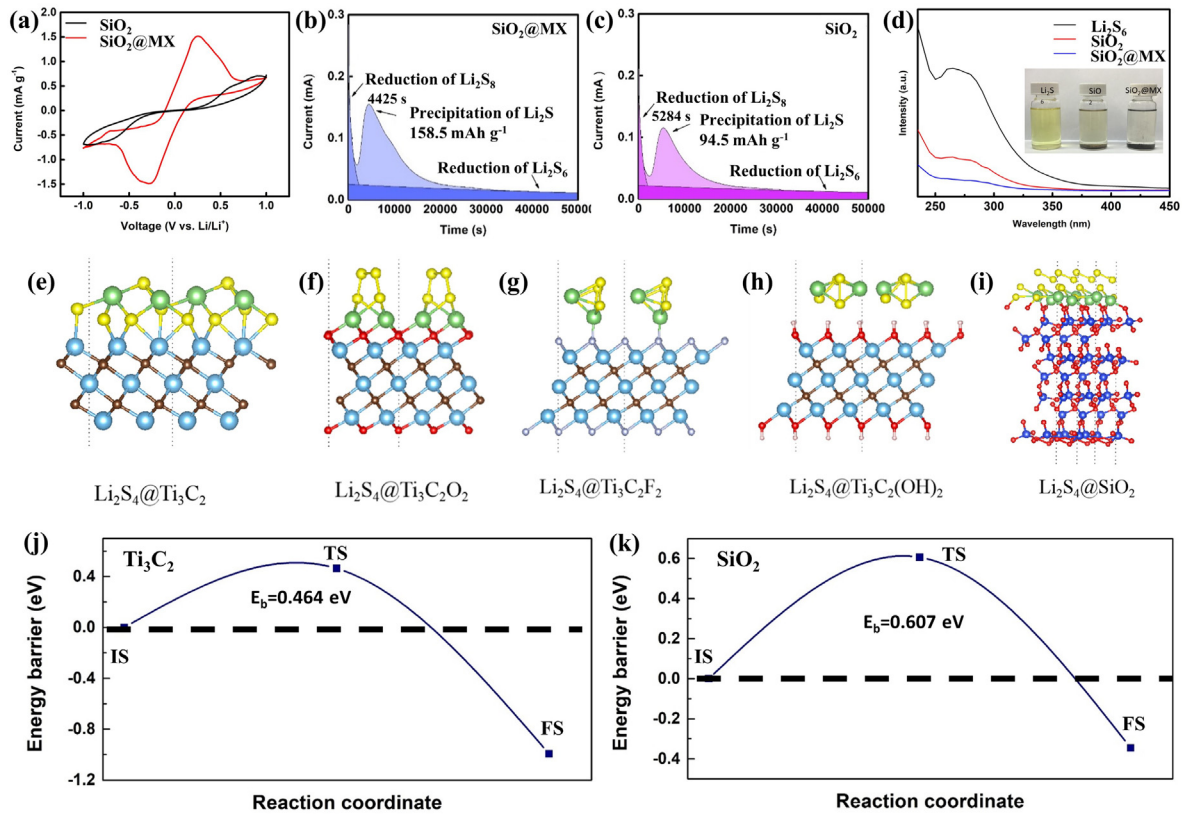
FIG. 4. (a) CV curves of the symmetric cells with SiO$_2$@MX/S and SiO$_2$/S cathodes. (b) and (c) Potentiostatic discharge profiles of Li$_2$S nucleation tests at 2.05 V. (d) Visual observation of the adsorption of Li$_2$S$_6$ with SiO$_2$@MX and SiO$_2$ and UV/vis absorption spectra after adsorption. (e)–(i) Adsorption structures of Li$_2$S$_4$ with Ti$_3$C$_2$, Ti$_3$C$_2$O$_2$, Ti$_3$C$_2$F$_2$, Ti$_3$C$_2$(OH)$_2$, and SiO$_2$. (j) and (k) Decomposition processes of Li$_2$S on Ti$_3$C$_2$ MXene and SiO$_2$, with insets of the initial state, transition state, and final state of the structures.
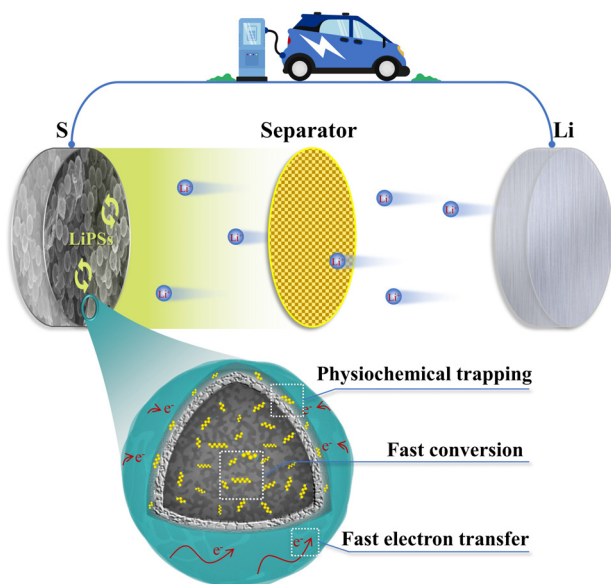
its unique core-shelled structure, together with the fast electron transfer and effective volume expansion buffer, the resulting Li–S battery exhibits excellent performance.

See the supplementary material for methods and Experimental data including additional SEM, EDS mapping, and TEM images, XRD, CV, electrochemical data, adsorption structures, and adsorption energies.

AUTHOR DECLARATIONS
Conflict of Interest

The authors have no conflicts to disclose.

Author Contributions

Chaoyue Zhang: Conceptualization (equal); Data curation (lead); Formal analysis (lead); Funding acquisition (lead); Writing – original

FIG. 5. Schematic illustration of Li–S battery configuration applying the SiO$_2$@MX/S cathode.

draft (lead). **Junan Feng:** Data curation (equal); Formal analysis (equal). **Xin Guo:** Data curation (equal); Formal analysis (equal). **Jinqiang Zhang:** Data curation (equal); Formal analysis (equal). **Wenxue Zhang:** Data curation (equal); Formal analysis (equal). **Lixue Zhang:** Data curation (equal); Formal analysis (equal); Writing – review & editing (equal). **Jianjun Song:** Conceptualization (lead); Funding acquisition (lead); Supervision (lead); Writing – review & editing (lead). **Guangjie Shao:** Conceptualization (equal); Funding acquisition (equal); Writing – review & editing (lead). **Guoxiu Wang:** Conceptualization (lead); Writing – review & editing (lead).

DATA AVAILABILITY

The data that support the findings of this study are available from the corresponding authors upon reasonable request.

REFERENCES

[1] R. Fang, S. Zhao, Z. Sun, D.-W. Wang, H.-M. Cheng, and F. Li, Adv. Mater. **29**, 1606823 (2017).

[2] Z. W. Seh, Y. Sun, Q. Zhang, and Y. Cui, Chem. Soc. Rev. **45**, 5605–5634 (2016).

[3] G. Zhou, H. Chen, and Y. Cui, Nat. Energy **7**, 312–319 (2022).

[4] X. Liu, J.-Q. Huang, Q. Zhang, and L. Mai, Adv. Mater. **29**, 1601759 (2017).

[5] F. Ma, K. Srinivas, X. Zhang, Z. Zhang, Y. Wu, D. Liu, W. Zhang, Q. Wu, and Y. Chen, Adv. Funct. Mater. **32**, 2206113 (2022).

[6] Z. Liang, W. Zhao, J. Shen, X. Xu, and J. Liu, Appl. Phys. Lett. **121**, 223904 (2022).

[7] J. Xu, Z. Lin, X. Huang, Y. Lei, C. Chen, and Z. Lin, Appl. Phys. Lett. **121**, 123902 (2022).

[8] J. Li, Z. Xiong, Y. Wu, H. Li, X. Liu, H. Peng, Y. Zheng, Q. Zhang, and Q. Liu, J. Energy Chem. **73**, 513–532 (2022).

[9] J. Huang, J. Huang, W. Chong, J. Cui, S. Yao, B. Huang, and J. Kim, J. Energy Chem. **35**, 204–211 (2019).

[10] K. Lu, H. Zhang, S. Gao, H. Ma, J. Chen, and Y. Cheng, Adv. Funct. Mater. **29**, 1807309 (2019).

[11] Z. Li, J. Zhang, B. Guan, D. Wang, L. Liu, and X. W. Lou, Nat. Commun. **7**, 13065 (2016).

[12] X. Liang, A. Garsuch, and L. F. Nazar, Angew. Chem., Int. Ed. **54**, 3907–3911 (2015).

[13] J. Song, X. Guo, J. Zhang, Y. Chen, C. Zhang, L. Luo, F. Wang, and G. Wang, J. Mater. Chem. A **7**, 6507–6513 (2019).

[14] F. Meng, H. Liu, B. Xu, S. Li, J. Liu, L. Liu, T. Gu, and H. Xiang, Appl. Phys. Lett. **121**, 123901 (2022).

[15] R. Hou, S. Zhang, Y. Zhang, N. Li, S. Wang, B. Ding, G. Shao, and P. Zhang, Adv. Funct. Mater. **32**, 2200302 (2022).

[16] X. Wang, D. Luo, J. Wang, Z. Sun, G. Cui, Y. Chen, T. Wang, L. Zheng, Y. Zhao, L. Shui, G. Zhou, K. Kempa, Y. Zhang, and Z. Chen, Angew. Chem., Int. Ed. **60**, 2371–2378 (2021).

[17] X. Guo, J. Zhang, J. Song, W. Wu, H. Liu, and G. Wang, Energy Storage Mater. **14**, 306–313 (2018).

[18] J. Li, J. Song, L. Luo, H. Zhang, J. Feng, X. Zhao, X. Guo, S. Chen, H. Liu, G. Shao, T. D. Anthopoulos, Y. Su, F. Wang, and G. Wang, Adv. Energy. Mater. **12**, 2200894 (2022).

[19] J. Li, H. Zhang, L. Luo, H. Li, J. He, H. Zu, L. Liu, H. Liu, F. Wang, and J. Song, J. Mater. Chem. A **9**, 2205–2213 (2021).